International Journal of Thermal Sciences 49 (2010) 809–819

Contents lists available at ScienceDirect

International Journal of Thermal Sciences

journal homepage: www.elsevier.com/locate/ijts

Investigation of weld pool in aluminum alloys: Geometry and solidification microstructure

A. Farzadi [a,*], S. Serajzadeh [b], A.H. Kokabi [b]

[a] Department of Materials Science and Engineering, Faculty of Engineering, Shahid Chamran University, Golestan Blvd., Ahvaz 11155-9466, Iran
[b] Department of Materials Science and Engineering, Sharif University of Technology, Azadi Ave., Tehran, Iran

ARTICLE INFO

Article history:
Received 5 January 2009
Received in revised form
2 November 2009
Accepted 8 November 2009
Available online 8 December 2009

Keywords:
Mathematical modeling
Heat transfer
Fluid flow
Electromagnetic force
GTA welding
Commercial pure aluminum
AA2017 aluminum alloy

ABSTRACT

In the present research, weld pool geometry, thermal cycle, temperature and velocity fields during gas tungsten arc welding of aluminum alloys were predicted by solving three-dimensional equations of conservation of mass, energy and momentum under steady-state conditions. Welding experiments were then conducted on several samples with different thicknesses and chemical compositions. The geometries of the weld pools as well as the thermal cycles were measured. It is found that the calculated geometry of the weld fusion zone and the weld thermal cycles are in good agreement with the corresponding experimental results. In addition, the magnitude of the maximum velocities under different conditions were estimated to understand the importance of heat transfer by convection and the roles of various driving forces in the weld pool. It is observed that the molten metal convection strongly affects on the weld pool geometry. A two vortex pattern due to the electromagnetic force and negative surface tension temperature gradient was coexisted in the weld pool. Finally, the predictions make it possible to estimate the morphology and the scale of the solidified structure through solidification parameter such as $G/\sqrt{R}$ and GR. The results show that as the welding speed increases, the value of $G/\sqrt{R}$ at the weld pool centerline decreases and tendency to develop an equiaxed microstructure increases.

1. Introduction

Since weld geometry and thermal cycles are influenced by thermal and fluid flow conditions [1–3], quantitative understanding of the heat transfer in the whole weldment as well as fluid flow in the weld pool is of importance to engineers and scientists. Beside, accurate prediction of the temperature and velocity fields is a prerequisite for modeling of various phase transformations such as solidification which takes place in welding processes [4,5]. To achieve this objective, it is necessary to develop a mathematical model including the equations of transport phenomena in the workpiece [6–8]. The equations are highly non-linear and coupled, so the numerical approach should be used to solve the coupled governing fluid flow, heat transfer and electromagnetic force equations. On the other hand, owing to the presence of the plasma in the vicinity of the weld pool and small size of the weld area, the experimental measurement of temperature and velocity fields are extremely difficult to perform [3,9]. Hence, numerical calculations of heat transfer and fluid flow have been realized to understand various weld characteristics that cannot be obtained otherwise as a practical recourse.

In the past two decades, the importance of convective heat transfer in the weld pool has been recognized and the different driving forces responsible for the fluid motion, such as surface tension gradient, electromagnetic, and buoyancy forces have been investigated in detail using mathematical modeling [6–8]. In the recent years, application of heat transfer and fluid flow has also been received special attention to achieve a better understanding of complex fusion welding processes and welded materials [9–19]. In many simple systems, numerical calculations of heat transfer and fluid flow are performed to obtain weld thermal cycles and the fusion zone (FZ) geometry [9–12]. The computed thermal cycles and/or temperature gradients have been used to quantitatively understand weldment microstructures and grain structures [13–15], the effect of surface-active element [16], inclusion characteristics [17], and concentrations of dissolved gases in the weld metal [18,19].

In this study, the heat transfer and fluid flow during gas tungsten arc (GTA) welding of aluminum alloys were modeled based on the fundamentals of transport phenomena and using a numerical heat transfer and fluid flow model [6,9]. The heat transfer and fluid flow calculation is focused on the predictions of the liquid metal convection in the weld pool, the temperature distribution in the

* Corresponding author. Tel./fax: +98 6113336642.
E-mail addresses: ali.farzadi@scu.ac.ir (A. Farzadi), serajzadeh@sharif.edu (S. Serajzadeh), kokabi@sharif.edu (A.H. Kokabi).

1290-0729/$ – see front matter © 2009 Elsevier Masson SAS. All rights reserved.
doi:10.1016/j.ijthermalsci.2009.11.007

whole weldment, and the shape and size of the FZ. Samples with different thicknesses have been considered for performing experiments and simulations. Verification of the model was carried out through comparing the calculated results with metallographic weld cross-sections and the weld thermal cycles. The order of magnitude analysis was conducted to understand the heat transfer mechanism. Also, several important solidification parameters, $G/\sqrt{R}$ and GR, including solidification rate R and temperature gradient G at the weld centerline and fusion line are predicted. These parameters may be used for determination of the solidification morphology and the scale of the solidification substructure. The effect of the welding speed on the solidification behavior within the FZ is also analyzed.

2. Mathematical model

The heat transfer and fluid flow in GTA welds were simulated using a three-dimensional (3-D), steady-state model. It is assumed that the liquid flow is Newtonian, laminar and incompressible and the problem is symmetric in the longitudinal plane along the welding direction. For determination of the velocity field in the weld pool and the temperature field in the whole workpiece, the equations of energy, mass and momentum conservation were considered. An enthalpy-porosity technique [20,21] is used for modeling the weld pool. The Marangoni effect caused by the surface tension gradient, and the electromagnetic and buoyancy body forces were taken to be driving forces of the weld pool convection. The following equations have been solved with the appropriate boundary conditions.

Mass conservation:

$$\nabla.(\rho \boldsymbol{u}) = 0 \tag{1}$$

Momentum conservation:

$$\nabla.(\rho \boldsymbol{u}\boldsymbol{u}) = -\nabla P + \nabla.(\mu \nabla \boldsymbol{u}) + \nabla.(\rho \boldsymbol{V}\boldsymbol{u}) + \boldsymbol{S} \tag{2}$$

where ρ is density, $\boldsymbol{u}$ is the velocity vector, μ is the viscosity, P is the pressure, $\boldsymbol{V}$ is the welding speed vector, which is only non-zero along the x-axis, $\boldsymbol{S}$ is the vector of source term for momentum equation. The mushy zone is modeled as a pseudo porous medium in which the porosity decreases from 1 to 0 as the material solidifies. When the material has fully solidified in a cell, the porosity becomes zero and hence the velocities also drop to zero. In Equation (2), the first term on the right-hand side is the pressure gradient. The fourth term, $\boldsymbol{S}$, can be expressed as follows [6,16]:

$$\boldsymbol{S} = -A\left[\frac{(1-f_L)^2}{f_L^3 + B}\right]\boldsymbol{u} + \rho \boldsymbol{g}\beta(T - T_{ref}) + \boldsymbol{S}_{emf} \tag{3}$$

where $\boldsymbol{g}$ is the gravitational acceleration vector, β is the thermal expansion coefficient, T is the temperature, T_{ref} is the reference temperature, f_L is the liquid fraction, B is a very small positive number, and A is a constant that represents mushy zone morphology and is a large number to cause the velocity components in the solid zone to be zero. In Equation (3), the first term on the right-hand side represents the frictional forces in the mushy zone according to the Carman–Kozeny equation for flow through a porous media. The second and third terms correspond to the buoyancy and the electromagnetic source terms, respectively. Boussinesq's approximation is used for the calculation of the buoyancy force [22]. The determination of the electromagnetic force is explained in detail below.

The other governing equation is energy conservation, which may be described as below:

$$\nabla.(\rho \boldsymbol{u}h) = \nabla.\left(\frac{k}{C_P}\nabla h\right) - \nabla.(\rho \boldsymbol{u}\Delta H) + \nabla.(\rho \boldsymbol{V}\Delta H) + \nabla.(\rho \boldsymbol{V}h) \tag{4}$$

where k is the thermal conductivity and C_P is the specific heat. In order to represent the solid/liquid interface, the total enthalpy H of the material is expressed as the sum of sensible heat h and latent heat content ΔH, i.e. $H = h + \Delta H$, where $h = \int C_P dT$, $\Delta H = f_L L$, L is the latent heat of fusion, and based on the level rule, the liquid fraction f_L is assumed to vary linearly with temperature in the mushy zone [6,21]. A 3-D Cartesian coordinate system is used in the calculation. Because of the symmetry about weld centerline [6,9], only one half of the workpiece is taken into account. The weld top surface is assumed to be flat. Also, the input heat on the top surface is assumed to obey a Gaussian distribution as follows [23]:

$$H_{in} = \frac{fQ\eta}{\pi r_b^2}\exp\left[-\left(\frac{f(x^2+y^2)}{r_b^2}\right)\right] \tag{5}$$

where r_b is the effective radius of the power distribution, f is the power distribution factor, Q is the total arc power and η is the power efficiency.

The velocity boundary conditions on the top surface are given as [6]:

$$\mu\frac{\partial u_x}{\partial z} = f_L\frac{d\gamma}{dT}\frac{\partial T}{\partial x}$$
$$\mu\frac{\partial u_y}{\partial z} = f_L\frac{d\gamma}{dT}\frac{\partial T}{\partial y}$$
$$u_z = 0 \tag{6}$$

where u_x, u_y, and u_z are the components of the velocity vector along the x, y, and z directions, respectively, and $d\gamma/dT$ is the temperature coefficient of surface tension. As shown in this equation, the u_x and u_y velocities are determined from the Marangoni effect. The u_z velocity is equal to zero since there is no outward flow at the pool top surface. Because of liquid fraction f_L, the shear stress is set equal to zero at the solid/mushy zone interface and increases linearly in the mushy zone. Heat losses by convection at the top surface are considered.

Symmetry boundary conditions are applied at the weld centerline ($y = 0$), as:

$$\frac{\partial u_x}{\partial y} = 0, \quad u_y = 0, \quad \frac{\partial u_z}{\partial y} = 0 \tag{7}$$

$$\frac{\partial h}{\partial y} = 0 \tag{8}$$

At all other surfaces, the heat losses by convection are considered and the initial velocities are set to be zero.

In arc welding, the electromagnetic or Lorentz force results from the interaction between the current flow and the self-induced magnetic field. Assuming that the electrical field is in a quasi-static state, the continuity equation for electrical charge and current is given by Gauss law as:

$$\nabla J = 0 \tag{9}$$

where J is the current density. For a linear isotropic conducting media, the current density is represented by Ohm's law as $J = \sigma E$ where E is the electrical field and σ is the electrical conductivity of the workpiece. Describing the electrical potential as $E = -\nabla\phi$ and using Equation (9), the electrical potential distribution, ϕ, in the workpiece is expressed as:

$$\nabla^2\phi = 0 \tag{10}$$

which is written in cylindrical coordinate system as:

$$\frac{\partial^2\phi}{\partial r^2} + \frac{\partial\phi}{r\partial r} + \frac{\partial^2\phi}{\partial Z^2} = 0 \tag{11}$$

where Z is the vertical distance from the bottom of workpiece. The current on the weld pool surface is assumed to obey a Gaussian distribution. Thus, boundary conditions for the potential field inside the workpiece are given by:

$$\phi(1,Z) = 0 \tag{12}$$

$$\frac{\partial\phi(r,0)}{\partial Z} = 0 \tag{13}$$

$$\frac{\partial\phi(0,Z)}{\partial r} = 0 \tag{14}$$

$$\frac{\partial\phi(r,t)}{\partial Z} = -\frac{Id}{\pi r_j^2\sigma}\exp\left(-\frac{r^2 d}{r_j^2}\right) \tag{15}$$

where l is the maximum radius, t is the thickness of the workpiece, I is the arc current, d is the current density distribution factor, and r_j is the effective radius of the current density distribution. Using separation of variables method, above boundary conditions and then substituting $Z = t - z$ to adapt with main coordinate system, the solution of Laplace Equation (11) can be expressed as:

$$\phi(r,z) = \sum_{n=1}^{\infty} A_n J_0(\lambda_n r)\cosh[\lambda_n(t-z)] \tag{16}$$

where λ_n are eigenvalues of the equation "$J_0(\lambda l) = 0$". Thus, $\lambda_n = \alpha_{0n}/l$ where α_{0n} are roots of zero order Bessel function.

A_n can be determined by inserting Equation (14) in Equation (15):

$$A_n = \frac{1}{\lambda_n \sinh(\lambda_n t)}\frac{2}{1^2 J_1^2(\lambda_n 1)}\int_0^1 rf(r)J_0(\lambda_n r)\mathrm{d}r \tag{17}$$

From the calculated potential field, the current density distribution can be obtained from Ohm's law:

$$J_r = -\sigma\frac{\partial\phi}{\partial r} \tag{18}$$

$$J_z = -\sigma\frac{\partial\phi}{\partial z} \tag{19}$$

Considering the axisymmetric condition, only the angular component of the self-induced magnetic flux vector, B_θ, is non-zero. Hence, the self-induced magnetic field by Ampere's law is presented as

$$B_\theta = \frac{\mu_m}{r}\int_0^1 J_z r\mathrm{d}r \tag{20}$$

Combining Equations (16)–(20), the components of the electromagnetic force vector $F = J \times B$ in the weld pool are calculated from:

$$F_x = -J_r B_\theta \cos\theta \tag{21}$$

$$F_y = -J_r B_\theta \sin\theta \tag{22}$$

$$F_z = -J_z B_\theta \tag{23}$$

where θ is the angle between the r-axis and the x-axis.

The model was applied to understand the temperature field and the weld dimensions for various GTA welding conditions. In addition, the weld pool geometry and various solidification parameters are calculated using temperature and velocity fields acquired from the utilized model.

3. Computational procedure

To numerically solve the governing equations with the associated source terms, a general computational fluid dynamics (CFD) computer program, FLUENT code was used. The material properties and workpiece information employed in the calculation of fluid flow and heat transfer are listed in Table 1 [24].

Accurate calculation of weld temperature and velocity fields, and the temperature gradients requires the use of a very fine grid system. A typical grid system used in the present study contained 143 × 73 × 50 grid points, and the corresponding computational domain had dimensions of 100 mm in length, 50 mm in width, and 5 mm and 10 mm in depth. Spatially non-uniform grids were used for maximum resolution of variables. Finer grid spacing was located near the heat source. The minimum grid spacing along the x and z directions were about 50 and 20 μm, respectively.

In order to enhance FLUENT code to compute the electromagnetic force, a user-defined function (UDF) is written in the C programming language by using Equations (16)–(23). The first fifty terms of the summation are considered for calculating components of the current density vector **J** and the magnetic field B_θ numerically. Finally, the computed electromagnetic force is applied to the momentum equation, Equation (2), as body force or source term, $\boldsymbol{S}_{emf}$.

4. Experimental procedure

AA1050 aluminum alloy plates with the thickness of 5 mm, the WA sample series, and 10 mm, the WB sample series, as well as an AA2017 aluminum alloy bar, WC sample series, were used in this investigation. GTA welds were performed on the aluminum plates using a 300 A direct constant current welding power supply with electrode negative polarity. The welding electrode was made of W-2%Th with 2.4 and 3.2 mm in diameter and high Purity (99.99%) argon was used as welding gas. The samples were machined out of the as-received materials. Then welding experiments were conducted under different conditions as listed in Table 2. After welding, the samples were cut and mounted along the top surface of the weld. All samples for optical microscopy (OM) examination were prepared by polishing to 1 μm finish. Microexamination of AA1050 aluminum alloy samples were realized by using electrolytic etching in Barker's reagent while AA2017 aluminum alloy samples were performed using chemical etching in Graff/Sargent reagent [25].

The thermal cycles were measured by using "K" thermocouples and an ADAM-4018 controller. The ADAM-4018 is a 16-bit, 8-channel analog input module that provides programmable input ranges on all channels. It uses a 16-bit microprocessor-controlled sigma-delta

Table 1
Physical properties of aluminum alloys used in the calculations [24].

Physical property	Value	
	AA1050	AA2017
Liquid temperature, T_L (K)	930	925
Solid temperature, T_S (K)	916	877
Density of liquid metal, ρ (kg/m^3)	2700	2750
Thermal conductivity of solid, k_S (J/m s K)	222	210
Thermal conductivity of liquid, k_L (J/m s K)	108	90
Specific heat of solid, C_{PS} (J/kg K)	904	900
Specific heat of liquid, C_{PL} (J/kg K)	904	900
Latent heat of melting, ΔH (J/kg)	3.95×10^5	3.95×10^5
Coefficient of thermal expansion, β (K^{-1})	2.55×10^{-5}	2.5×10^{-5}
Temperature coefficient of surface tension, $d\gamma/dT$ (N/m K)	-0.152×10^{-3}	-0.149×10^{-3}
Magnetic permeability, μ_m (N/A^2)	1.26×10^{-6}	1.26×10^{-6}

Table 2
Conditions of GTA welded samples.

Variables	Thickness (mm)	Current (A)	Voltage (V)	Welding speed (mm/s)
WA1	5	110	15	3
WA2	5	110	15	4
WA3	5	110	15	5
WA4	5	110	15	6
WA5	5	110	15	7
WB1	10	150	17	3
WB2	10	150	17	4
WB3	10	150	17	5
WB4	10	150	17	6
WB5	10	150	17	7
WC1	5	110	15	3
WC2	5	110	15	8

A/D converter to convert sensor voltage or current into digital data. The digital data is then translated into engineering units. When prompted by the host computer, the module sends the data to the host through a standard RS-485 interface. Type K thermocouples (chromel alumel) were used in all tests. They are the most commonly used thermocouples and support oxidizing atmospheres. Electrical insulation of the thermocouple was achieved by protecting its measuring part with a thin alumina-based tube. Temperatures were acquired at two points in the middle of plate thickness. Thermocouples are set into holes, made in perpendicular to the weldment line and with different depths.

5. Results and discussion

5.1. Weld pool geometries

Figs. 1(a)–(f), 2(a)–(f) and 3(a), (b) show the comparison between the measured and calculated geometries of the FZ in the weld pool cross-section for the samples WA1–WA5, WB1–WB5 and WC1–WC2, respectively. In these figures, the mushy zone, i.e. the solid and liquid two phase region, is presented with the distinct color. Note that the mushy zone is determined as the region having temperature between the solidus and liquidus isotherms. As shown in these figures, the computed weld pool geometries and dimensions agree well with the corresponding experimental results.

Fig. 4(a) and (b) indicates the calculated velocity vectors of the samples WA1 and WB1, respectively. It is observed that each velocity field is composed of two vortexes: in the left view, one is clockwise and near the center, caused by the electromagnetic force; and the other is counterclockwise and nearly parallel to the top free surface, caused by the negative temperature coefficient of surface tension ($d\gamma/dT < 0$). There is a difference in velocity scale between these two vortexes. Due to the assumed Gaussian distribution of the incident thermal flux, the maximum surface temperature occurs at the center of the weld pool, as indicated in Fig. 5. Hence, the surface tension increases outward from the center as the temperature decreases outward, causing the liquid metal at the surface to flow outward, and creating the counterclockwise vortex and the width of the weld pool. The outward flow at the surface can be better seen from the corresponding top-viewed flow patterns and isotherms, shown in Fig. 5. On the other hand, the clockwise vortex carries heat from the top surface downward, creating pool penetration, although it is small under the present conditions. Hence, the weld pool exhibits shallow penetration and a large width-to-depth ratio for all samples, as illustrated in Fig. 6. Therefore, it is found that the fluid flow in the weld pool is highly complex and has a significant effect on the weld pool temperature distribution and the development of the weld pool shape and size.

It is observed that the velocity scale of the clockwise vortex for the sample WB1 is smaller than that for the sample WA1 by comparing Fig. 4(a) and (b), although the velocity vectors of the counterclockwise vortex for these samples are comparable in size and the welding current used for the sample WB1 is higher than that for the sample WA1. If electromagnetic force is the only driving force for the liquid convection, an order of magnitude of the maximum velocity (u_{emf}) under electromagnetic convection is given by [7]:

$$u_{emf} = \frac{DI}{2\pi r_b^2}\sqrt{\frac{10\mu_m D}{\rho t}} \tag{24}$$

where D is the pool depth, I is the arc current, μ_m is the magnetic permeability, and t is the thickness of the workpiece. The magnitude of the maximum velocity under electromagnetic driven flow for the samples WA1 and WB1 are 123.7 mm/s and 65.2 mm/s, respectively. Although, in the case WB1, the welding current is increased to 150 A but the effective radius of the power distribution, r_b, and the effective radius of the current density distribution, r_j, for the sample WA1 are smaller than those for the sample WB1 because of the smaller size of tungsten electrode as well as the sample WB1 has the higher thickness. According to Equation (24), these changes lead to a decrease in u_{emf}. From physical point of view, the peak current density on the top surface of the case WB1, which is the source of the current density for the workpiece (see Equation (15)), is lower than that of the case WA1. Besides, the lower current density distributes in the bigger area due to the higher thickness of the case WB1. As a result, the increase in the welding current for the case WB1 is not enough to compensate the decrease in the electromagnetic force due to r_b and thickness. Furthermore, since the different driving forces play important role in dissipating the heat in the weld pool and determine the temperature distribution in the weld pool, it can be concluded that the shallow weld pool of the sample WB1 caused by the smaller current density distribution and the electromagnetic force.

5.2. Weld thermal cycles

The variation of temperature with time i.e. the thermal cycle, may lead to various solid-state phase transformations. Temperature as a function of time at different locations (x, y, z) can be calculated by using the predicted temperature field as [6]:

$$T(x,y,z,t_2) = \frac{T(\xi_2,y,z) - T(\xi_1,y,z)}{\xi_2 - \xi_1} V(t_2 - t_1) + T(x,y,z,t_1) \tag{25}$$

where $T(\xi_2, y, z)$ and $T(\xi_1, y, z)$ are the steady-state temperatures at coordinates (ξ_2, y, z) and (ξ_1, y, z), respectively; $(\xi_2 - \xi_1)$ is the distance traveled by the torch in time $(t_2 - t_1)$; and $T(x, y, z, t_1)$ and $T(x, y, z, t_2)$ are the temperatures at location (x, y, z) at times t_1 and t_2, respectively.

The comparison between the measured and calculated weld thermal cycles at two different locations is provided in Fig. 7(a) and (b). In these figures, the measured thermal cycles are plotted as solid dots, while the calculated thermal cycles are represented by the solid lines. Although the thermocouple data does not lie on the calculated ones, good agreement between the computed and experimental curves indicates the validity of the heat transfer and fluid flow model.

Fig. 8 shows the calculated thermal cycles at the weld centerline for the samples WA1 and WB1. From Fig. 8, it can be seen that the peak temperature of the sample WA1 is less than that of the sample WB1 due to higher heat input.

In Fig. 9, the calculated thermal cycles at the centerline for the samples WC1 and WC2 are presented. The sample WC2 is subjected to higher heating and cooling rates. Moreover, the weld pool of the

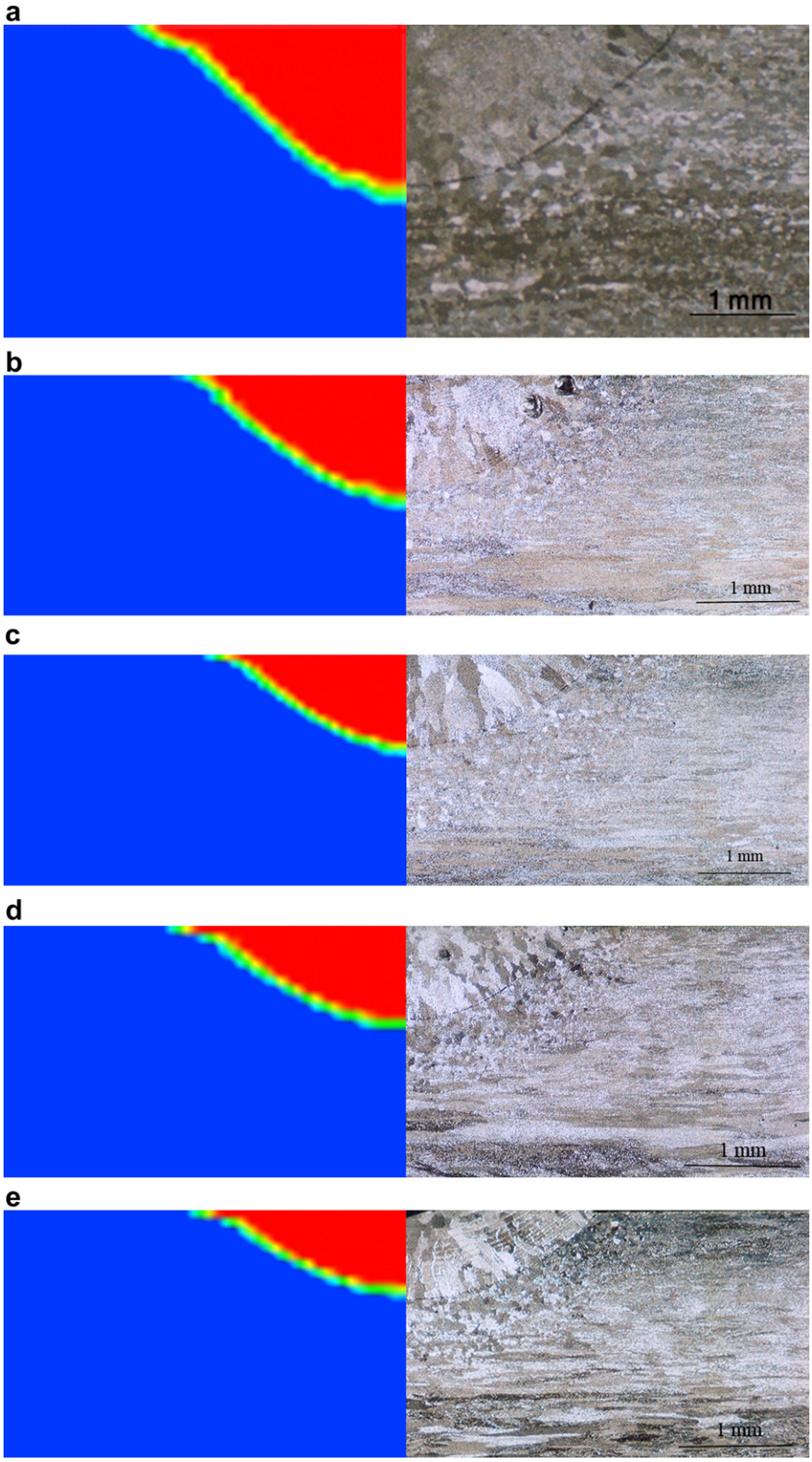

Fig. 1. Experimental and calculated weld pool cross-sections for GTA welds obtained by using conditions of samples (a) WA1; (b) WA2; (c) WA3; (d) WA4; and (f) WA5.

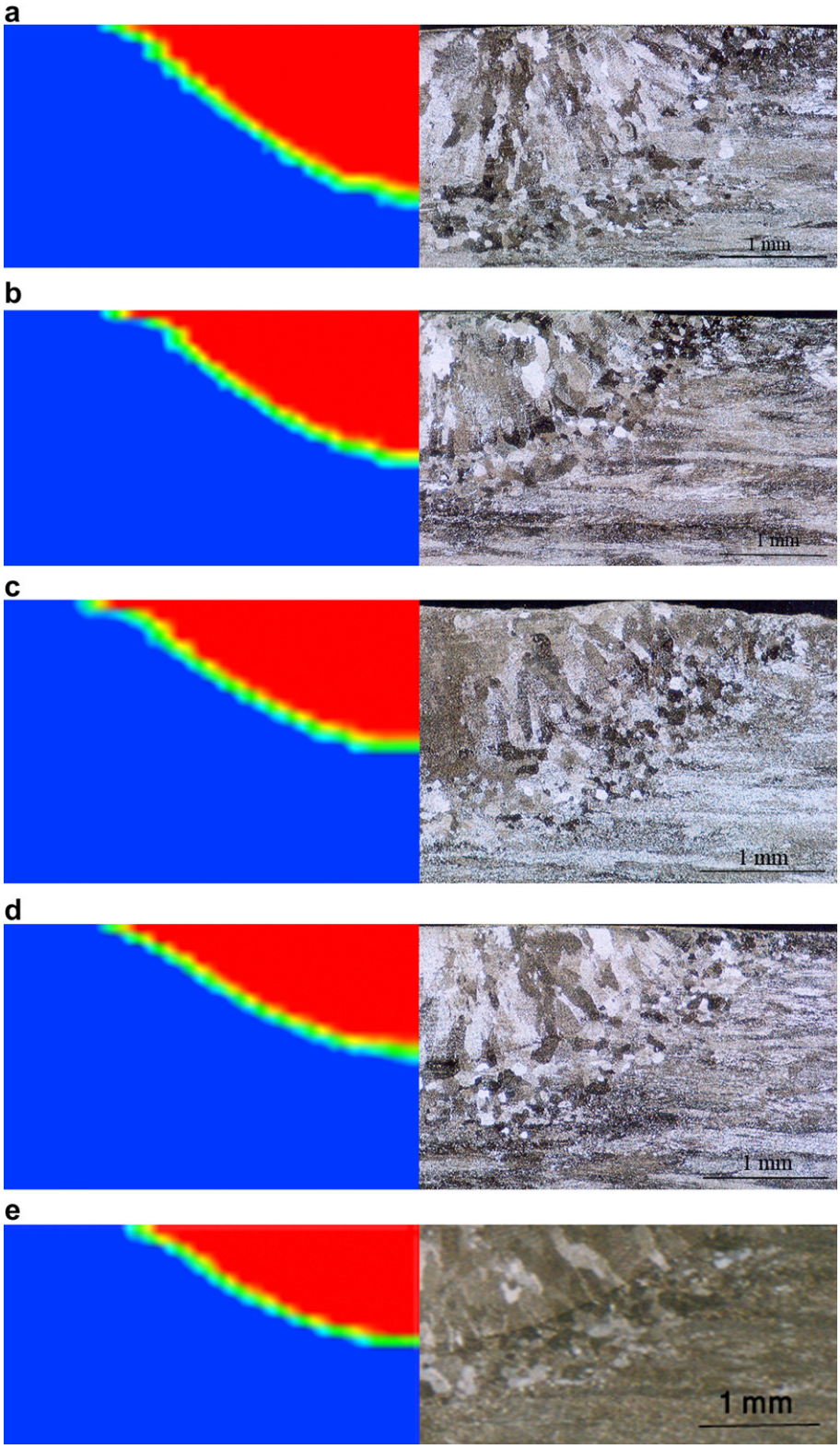

Fig. 2. Experimental and calculated weld pool cross-sections for GTA welds obtained by using conditions of samples (a) WB1; (b) WB2; (c) WB3; (d) WB4; and (f) WB5.

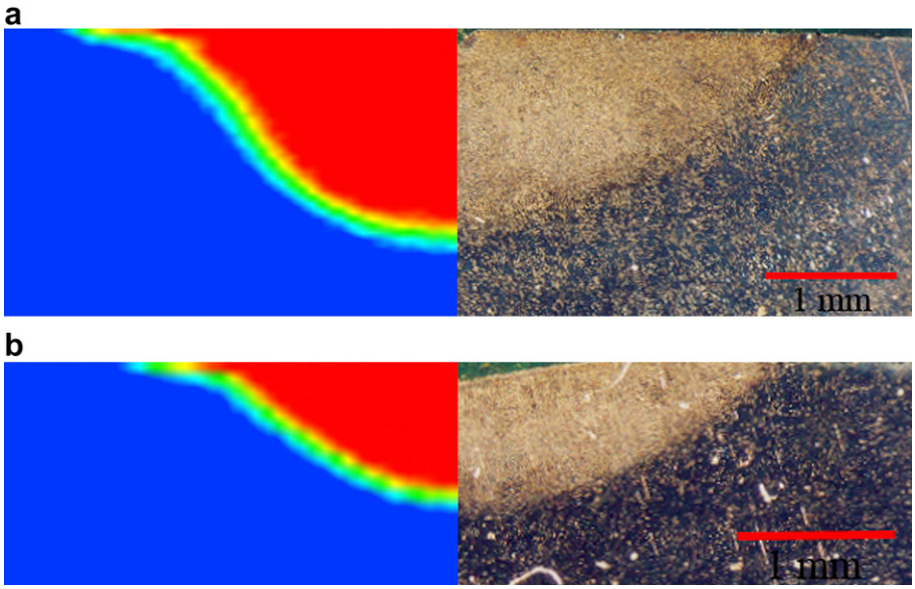

Fig. 3. Experimental and calculated weld pool cross-sections for GTA welds obtained by using conditions of samples (a) WC1; and (b) WC2.

sample WC1 has higher peak temperature. These features originate from the less welding speed and the higher heat input of the sample WC1. As can be seen in Figs. 8 and 9, during the heating and cooling periods, there are inflection points at liquidus temperature in the thermal cycle curve. This may be attributed to the differences in the enthalpies of the solid and the liquid metals.

5.3. Solidification microstructure

Because of the similarities between the solidification behavior of castings and welds, parameters important in determining cast microstructures such as growth rate (R), temperature gradient (G), undercooling (ΔT), and alloy constitution are also useful for determination of the development of microstructures in welds. Since weld solidification proceeds from the preexisting solid substrate, only undercooling associated with growth is important. The undercooling is comprised of contributions from thermal, constitutional, kinetic and solid curvature effects. In this study, the effect of undercooling has been ignored and therefore, the solidification parameters were calculated by considering only the heat transfer and fluid flow in the weld pool. In other word, the equilibrium liquidus isotherm is assumed to represent the liquid/mushy boundary, while the equilibrium solidus isotherm was assumed to be the mushy zone/solid boundary.

As shown in Fig. 10, the average temperature gradient at the weld centerline, $\overline{G}_{CL}$, and the fusion line, $\overline{G}_{FL}$, of the weld pool along a given plane is defined as:

$$\overline{G}_{CL} = \frac{T_P - T_L}{c} \tag{26}$$

$$\overline{G}_{FL} = \frac{T_C - T_L}{d} \tag{27}$$

where T_P is the peak temperature, T_L is the liquidus temperature, T_C is the maximum temperature in directions perpendicular to the

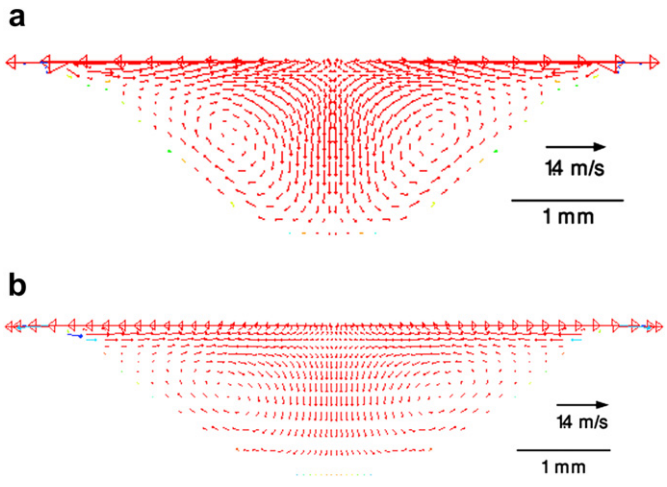

Fig. 4. Calculated velocity vector of the weld pool cross-section for samples (a) WA1; and (b) WB1.

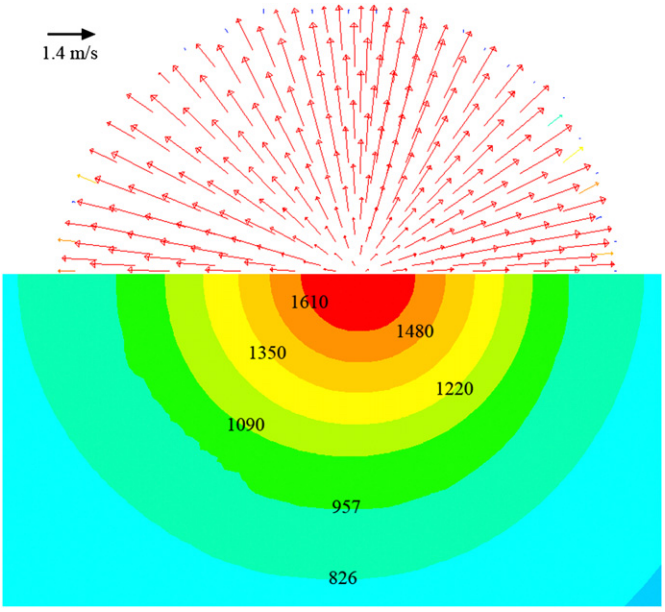

Fig. 5. Velocity vectors and temperature field on the top surface of sample WA1.

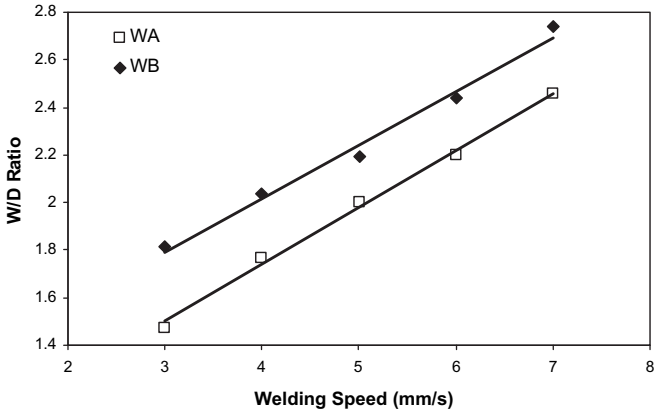

Fig. 6. Effects of welding speed on ratio of half width-to-depth of weld pools.

fusion boundary where the maximum width has been occurred, "c" is the distance between the location of peak temperature and boundary at the weld pool centerline and "d" is the distance between the location of T_C and the fusion line. Fig. 11(a) and (b) shows the average temperature gradients at the weld centerline ($\overline{G}_{CL}$) and the fusion line ($\overline{G}_{FL}$) for the WA and WB sample series, respectively. These figures illustrate that both $\overline{G}_{FL}$ and $\overline{G}_{CL}$ decrease as welding speed increases and $\overline{G}_{FL}$ is higher than $\overline{G}_{CL}$($\overline{G}_{FL} > \overline{G}_{CL}$). The similar behavior is shown in the literature [1]. It is also observed that $\overline{G}_{FL}$ gets closer to $\overline{G}_{CL}$ in the higher welding speeds for the WA sample series but not for the WB sample series. These behaviors are resulted from the increase in the weld pool size and

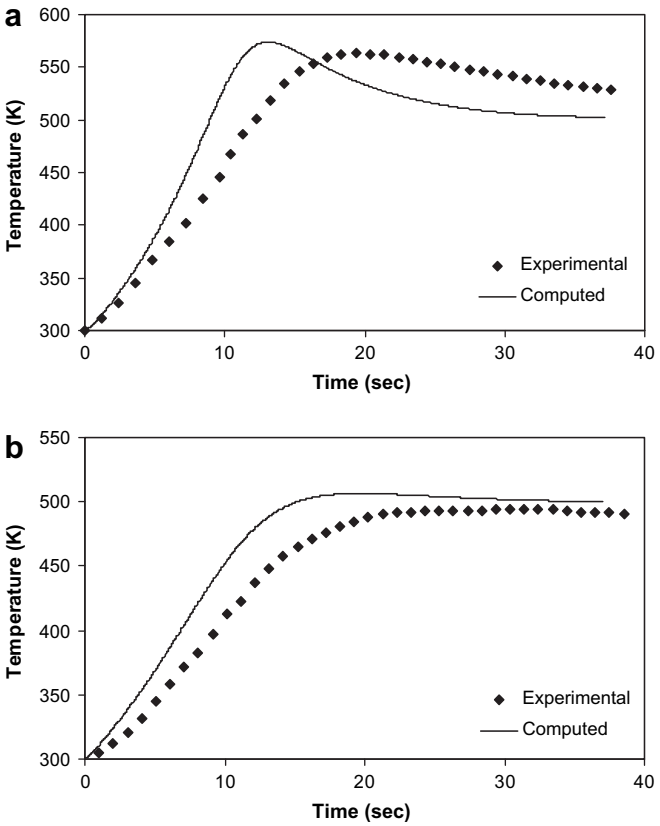

Fig. 7. Comparison between the measured and calculated weld thermal cycles for sample WA1 at distance of (a) 10 mm and (b) 20 mm from the centerline.

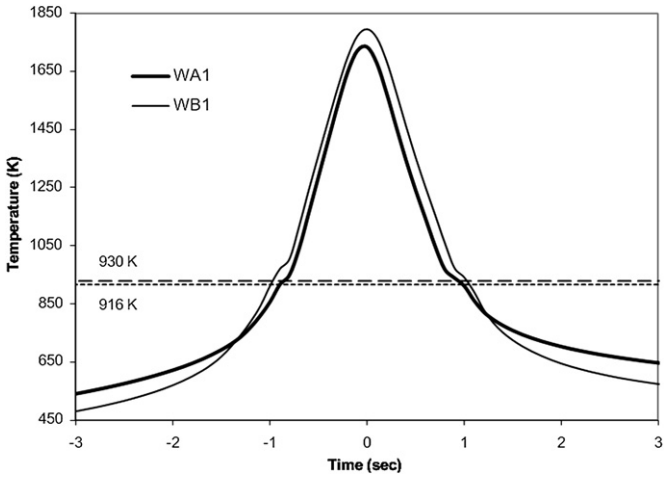

Fig. 8. Calculated thermal cycles for GTA welds obtained by using condition of samples WA1 and WB1 at the weld centerline.

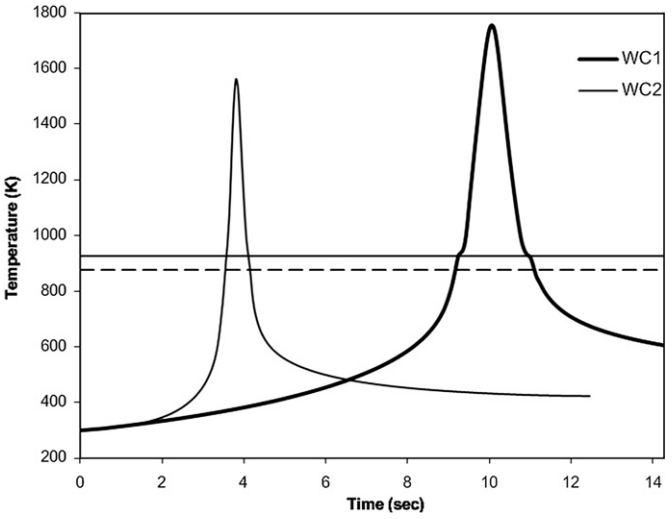

Fig. 9. Computed thermal cycles at weld centerline for samples WC1 and WC2.

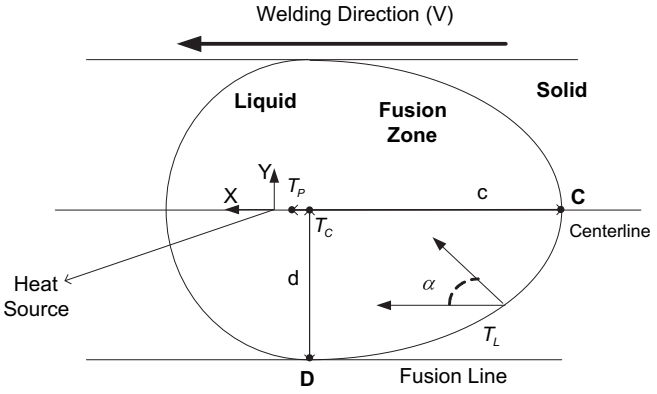

Fig. 10. A schematic plot showing location of heat source, peak temperature, calculation of average temperature gradients at weld centerline and fusion line.

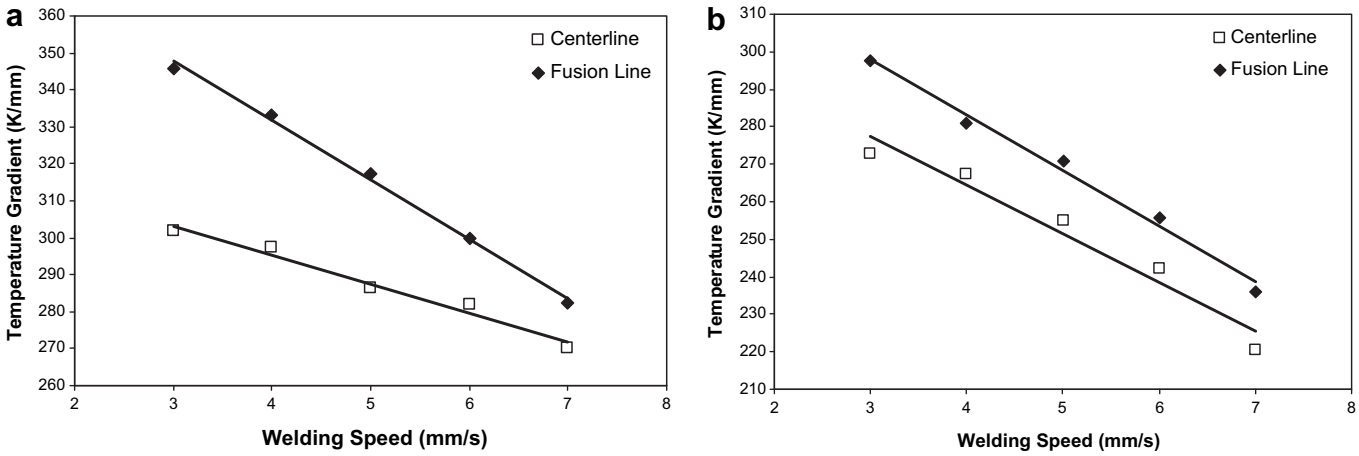

Fig. 11. Calculated values of average temperature gradients at weld pool centerline and fusion line with different welding speed for (a) WA and (b) WB sample series.

the decrease in the temperature gradient. It should be mentioned that this result is true for particular welding conditions considered in the present work. If decreasing rate of the weld pool size is higher than decreasing rate of the peak temperature, the temperature gradient may be altered in a different manner.

Since the shape of the weld pool remains constant under steady-state conditions, therefore, the solidification rate varies with position along the fusion boundary. The direction of movement of the solidification front is along the maximum thermal gradient normal to the solid/liquid interface, as shown in Fig. 10. The steady state solidification rate, R, is related to the welding speed as [3]

$$R = V\cos\alpha \tag{28}$$

where α is the angle between the normal to the solid/liquid interface and the welding direction and V is the welding speed. The solidification rate increases from the edge of the weld pool ($\alpha \rightarrow 90^{\circ}$), indicated by point D in Fig. 10, to point C on the weld centerline ($R_{CL} = V$) along the fusion boundary. Therefore, the solidification rate at the fusion line is zero ($R_{FL} = 0$) and $R_{CL} \gg R_{FL}$.

The temperature gradient and the solidification rate are important in the combined forms $G/\sqrt{R}$ and GR as they influence the solidification morphology and the scale of the solidification substructure, respectively. As already mentioned, $\overline{G}_{FL} > \overline{G}_{CL}$ and $R_{CL} \gg R_{FL}$. Consequently,

$$\left(\frac{G}{\sqrt{R}}\right)_{CL} \ll \left(\frac{G}{\sqrt{R}}\right)_{FL} \tag{29}$$

$$(G \times R)_{CL} > (G \times R)_{FL} \tag{30}$$

As a result, the value of $G/\sqrt{R}$ decreases from the fusion line to the weld center. As the value of $G/\sqrt{R}$ increases, the interface morphology changes from equiaxed-dendritic, to cellular-dendritic, to cellular grains [3]. Often the value of $G/\sqrt{R}$ close to the fusion line is large enough to facilitate cellular solidification, as can be seen in Fig. 12(a). Hence, it is expected a cellular type of microstructure close to the fusion line, an equiaxed-dendritic microstructure at the pool center, and cellular-dendritic microstructure between these two regions. Fig. 12(b) demonstrates the equiaxed grain at the weld centerline. An important variable in determining the weld pool microstructural characteristic is the cooling rate ($G \times R$) which is the product of the temperature gradient G and the growth rate R. According to Equation (30), the cooling rate at the weld centerline is higher than the cooling rate at the fusion line. This suggests that the dendrite arm spacing decreases from the fusion line to the centerline because the dendrite arm spacing decreases with increasing cooling rate.

As can be seen in Fig. 13(a) and (b), with increasing in the welding speed from 3 mm/s to 8 mm/s, the value of $G/\sqrt{R}$ decreases from

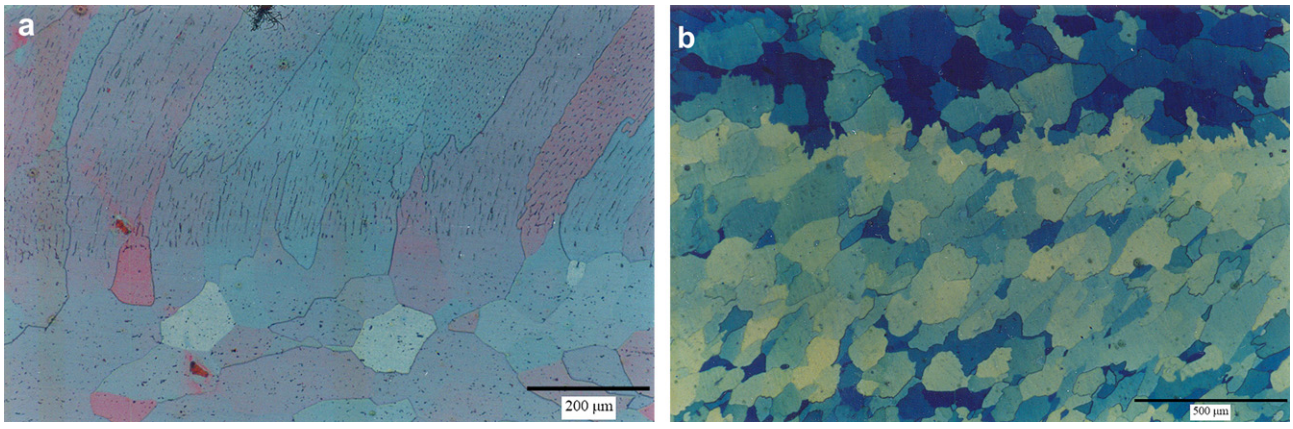

Fig. 12. Weld pool microstructures: (a) fusion line and (b) centerline for sample WA1.

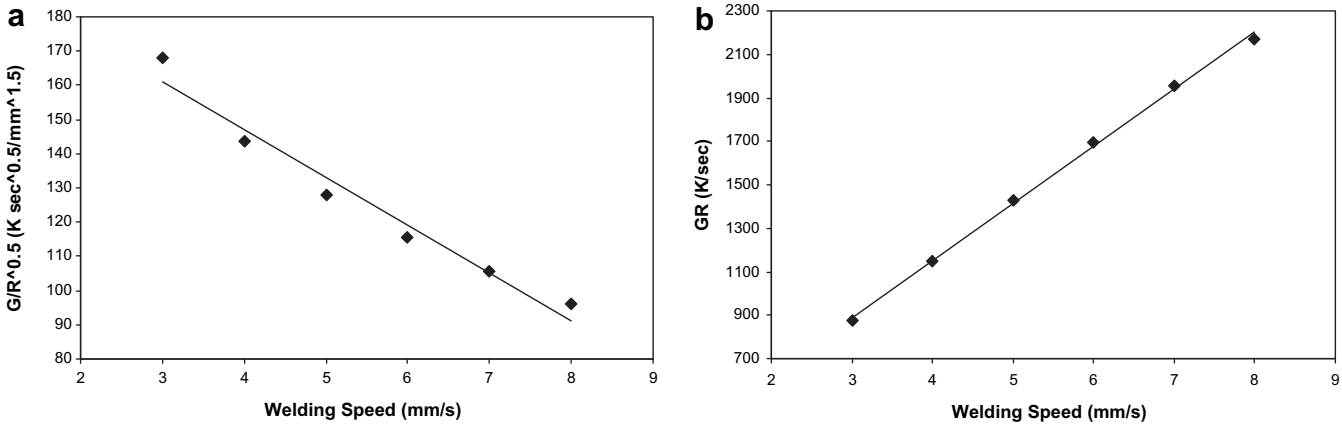

Fig. 13. Calculated values of (a) $G/\sqrt{R}$ and (b) GR at weld pool centerline with different welding for AA2017.

168 K $s^{0.5}$ $mm^{-1.5}$ to 96 K $s^{0.5}$ $mm^{-1.5}$, and the value of GR increases from 873 K/s to 2171 K/s for AA2017 aluminum alloy GTA welds. Thus, it is expected that there is a higher tendency to develop an equiaxed-dendritic microstructure in higher welding speeds. Several authors have reported that grain boundaries, mainly of columnar grains, are particularly sensitive to cracking [5]. On the other hand, equiaxed microstructure shows better resistance to crack formation and propagation. Furthermore, finer microstructure can be obtained by using higher welding speeds, as represented in Fig. 14(a) and (b). Therefore, solidification structure of fusion zone would be affected by the welding speed considerably.

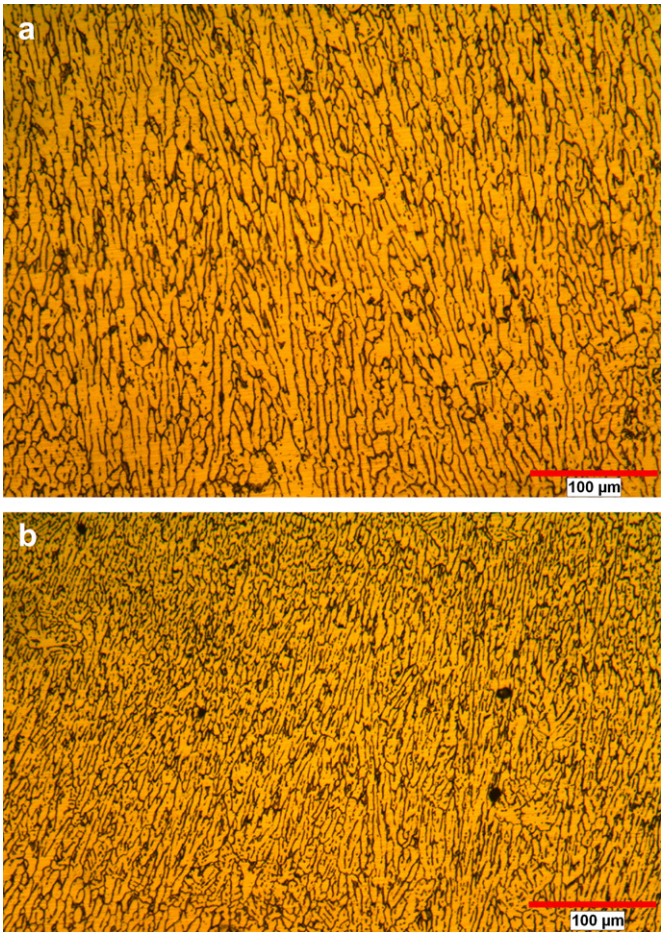

Fig. 14. Microstructures of AA2017 weld pools obtained by using 110 A, 15 V, and (a) 3 mm/s and (b) 8 mm/s at the centerline.

6. Conclusion

The weld pool shape and size, temperature and velocity fields, weld thermal cycles, and the solidification parameters during GTA welding of aluminum alloys were quantitatively obtained by using a comprehensive 3-D heat transfer and fluid flow model. Under the analogous conditions, experiments were performed to verify the model results. The following conclusions can be made from the investigation:

(1) The geometry of the FZ and weld thermal cycles for the samples with different thicknesses and chemical compositions predicted by using FLUENT code are in a good agreement with the corresponding experimental results.
(2) A double-loop circulation pattern was acquired in the GTA weld pools of AA1050 aluminum alloy: one is near the center; and the other is nearly parallel to the top free surface induced by the electromagnetic force; and the negative surface tension temperature gradient ($d\gamma/dT < 0$), respectively.
(3) The velocity vectors and the magnitudes of the maximum velocities show that higher thickness and lower input current density of the WB sample series results in smaller electromagnetic force. Hence, the WB sample series have larger width-to-depth ratio.
(4) The solidification parameters including temperature gradient G, solidification rate R and the combined forms $G/\sqrt{R}$ and GR were quantitatively calculated and then used to estimate the solidification morphology and substructure in GTA welds under the different conditions. The values of $G/\sqrt{R}$ decrease from 174 K $s^{0.5}$ $m^{-1.5}$ to 102 K $s^{0.5}$ $m^{-1.5}$ for the WA sample series, and therefore resistance to crack formation and propagation increases as the welding speed increases.

References

[1] J.F. Lancaster, Metallurgy of Welding, sixth ed. Abington, Cambridge, 1999.
[2] K. Easterling, Introduction to the Physical Metallurgy of Welding, second ed. Butterworths, 1992.
[3] S. Kou, Welding Metallurgy, second ed. John Wiley and Sons, Hoboken, New Jersey, 2003.
[4] S.A. David, S.S. Babu, J.M. Vitek, Welding: solidification and microstructure. JOM-Journal of the Minerals Metals and Materials Society 55 (2003) 14–20.
[5] S.A. David, J.M. Vitek, Correlation between solidification parameters and weld microstructures. International Materials Reviews 34 (1989) 213–245.

[6] K. Mundra, T. DebRoy, K.M. Kelkar, Numerical prediction of fluid flow and heat transfer in welding with a moving heat source. Numerical Heat Transfer, Part A 29 (1996) 115–129.
[7] G.M. Oreper, J. Szekely, A comprehensive representation of transient weldpool development in spot welding operations. Metallurgical Transactions A 18A (1987) 1325–1332.
[8] I.S. Kim, A. Basu, A mathematical model of heat transfer and fluid flow in the gas arc welding process. Journal of Materials Processing Technology 77 (1998) 17–24.
[9] G. Amberg, M. Do-Quang, Thermocapillary convection and phase change in welding. International Journal of Numerical Methods for Heat and Fluid Flow 18 (2008) 378–386.
[10] S. Wang, J. Goldak, J. Zhou, S. Tchernov, D. Downey, Simulation on the thermal cycle of a welding process by space–time convection–diffusion finite element analysis. International Journal of Thermal Sciences 48 (2009) 936–947.
[11] A. Farzadi, S. Serajzadeh, A.H. Kokabi, Modeling of heat transfer and fluid flow during gas tungsten arc welding of commercial pure aluminum. International Journal of Advanced Manufacturing and Technology 38 (2008) 258–267.
[12] S. Kou, Y.H. Wang, Three dimensional convection in laser melted pools. Metallurgical Transactions A 17A (1986) 2265–2270.
[13] M.-Y. Li, J.R.E. Kannatey-Asibu, Monte Carlo simulation of heat-affected zone microstructure in laser-beam-welded nickel sheet. Welding Journal 81 (2002) 37S–44S.
[14] A. Farzadi, M. Do-Quang, S. Serajzadeh, A.H. Kokabi, G. Amberg, Phase-field simulation of weld solidification microstructure in an Al–Cu alloy. Modelling and Simulation in Materials Science and Engineering 16 (2008) No. 065005.
[15] V. Pavlyk, U. Dilthey, Simulation of weld solidification microstructure and its coupling to the macrostructure heat and fluid flow modelling. Modelling and Simulation in Materials Science and Engineering 12 (2004) S33–S45.
[16] Y. Wang, Q. Shi, H.L. Tsai, Modeling of the effects of surface-active elements on flow patterns and weld penetration. Metallurgical and Materials Transactions B 32B (2001) 145–161.
[17] T. Hong, T. DebRoy, Nonisothermal growth and dissolution of inclusions in liquid steels. Metallurgical Transactions B 34B (2003) 267–269.
[18] H. Zhao, T. DebRoy, Weld metal composition change during conduction mode laser welding of aluminum alloy 5182. Metallurgical Transactions B 32B (2001) 163–172.
[19] A.D. Zervaki, G.N. Haidemenopoulos, Computational kinetics simulation of the dissolution and coarsening in the HAZ during laser welding of 6061-T6 Al-alloy. Welding Journal 86 (2007) 211s–221s.
[20] A.D. Brent, V.R. Voller, K.J. Reid, Enthalpy-porosity technique for modeling convection–diffusion phase-change – application to the melting of a pure metal. Numerical Heat Transfer 13 (1988) 297–318.
[21] FLUENT User's Guide. FLUENT Inc., 2006.
[22] A. Kumar, T. DebRoy, Calculation of three-dimensional electromagnetic force field during arc welding. Journal of Applied Physics 94 (2003) 1267–1277.
[23] N.S. Tsai, T.W. Eager, Distribution of the heat and current fluxes in gas tungsten arcs. Metallurgical Transactions B 16B (1985) 841–846.
[24] J.E. Hatch, Aluminum: Properties and Physical Metallurgy. American Society for Metals International, Metals Park, OH, 1984.
[25] Metals Handbook, vol.13, ninth ed. American Society for Metals International, Metals Park, OH, 2001.